Boosting Electrocatalytic Carbon Dioxide Reduction via Self-Relaxation of Asymmetric Coordination in Fe-Based Single Atom Catalyst

Zhaoyong Jin, Dongxu Jiao, Yilong Dong, Lin Liu, Jinchang Fan, Ming Gong, Xingcheng Ma, Ying Wang, Wei Zhang, Lei Zhang, et al.

doi.org/10.1002/anie.202318246

Boosting Electrocatalytic Carbon Dioxide Reduction via Self-Relaxation of Asymmetric Coordination in Fe-Based Single Atom Catalyst

Zhaoyong Jin[+], Dongxu Jiao[+], Yilong Dong, Lin Liu, Jinchang Fan, Ming Gong, Xingcheng Ma, Ying Wang, Wei Zhang, Lei Zhang, Zhi Gen Yu, Damien Voiry, Weitao Zheng,* and Xiaoqiang Cui**

Abstract: Addressing the limitations arising from the consistent catalytic behavior observed for various intermediates during the electrochemical carbon dioxide reduction reaction (CO_2RR) poses a significant challenge in the optimization of catalytic activity. In this study, we aimed to address this challenge by constructing an asymmetric coordination Fe single atom catalyst (SCA) with a dynamically evolved structure. Our catalyst, consisting of a Fe atom coordinated with one S atom and three N atoms ($Fe—S_1N_3$), exhibited exceptional selectivity (CO Faradaic efficiency of 99.02 %) and demonstrated a high intrinsic activity (TOF of 7804.34 h^{-1}), and remarkable stability. Using operando XAFS spectra and Density Functional Theory (DFT) calculations, we elucidated the self-relaxation of geometric distortion and dynamic evolution of bond lengths within the catalyst. These structure changes enabled independent regulation of the *COOH and *CO intermediate adsorption energies, effectively breaking the linear scale relationship and enhancing the intrinsic activity of CO_2RR. This study provides valuable insights into the dynamic evolution of SACs and paves the way for targeted catalyst designs aimed to disrupt the linear scaling relationships.

Introduction

The electrochemical reduction of carbon dioxide (CO_2RR) to produce value-added chemicals using electricity from renewable sources offers a cleaner and more sustainable pathway towards carbon neutrality. This technology holds great promise in mitigating greenhouse effects and addressing energy shortages.[1] Nevertheless, the energy efficiency and selectivity of CO_2RR still fall short of practical industrialization requirements.[2] Therefore, it is crucial to rationally design CO_2RR catalysts and establish a comprehensive understanding of the structure-property correlations in this field.[2b,3]

Recently, atomically dispersed single-atom catalysts (SACs) with well-defined active sites and the utmost theoretical atom utilization have demonstrated remarkable CO_2RR performance.[4] They are also widely recognized as exemplary model systems for investigating catalytic mechanisms at the atomic level.[5] Nevertheless, CO_2RR is a complex heterogeneous catalytic process involving a multitude of intermediates and proton coupling pathways.[6] Due to the simplicity of the SACs structure, there are inherent limitations in overcoming the linear scaling relationship associated with different intermediates.[7] Taking the CO_2 reduction to CO as an example, catalysts must enhance the adsorption energy of *COOH intermediates to promote proton coupling while weakening the adsorption of *CO intermediates to facilitate product desorption.[8] However, the intricate correlation between the active sites and intermediates' adsorption energy impedes the simultaneous optimization of both aspects.[7b,9] Despite the recent advance-

[*] Z. Jin,[+] D. Jiao,[+] Y. Dong, L. Liu, J. Fan, M. Gong, X. Ma, Y. Wang, W. Zhang, W. Zheng, Prof. Dr. X. Cui
School of Materials Science and Engineering, Key Laboratory of Automobile Materials of MOE, Electron Microscopy Center, Jilin University
130012 Changchun (China)
E-mail: wtzheng@jlu.edu.cn
xqcui@jlu.edu.cn
Prof. L. Zhang
College of Chemistry, Jilin University
130012 Changchun (China)
E-mail: lzhang@jlu.edu.cn
Prof. Dr. Z. Gen Yu
Institute of High Performance Computing (IHPC), Agency for Science, Technology and Research (A*STAR)
1 Fusionopolis Way, #16-16 Connexis, 138632 Singapore (Singapore)
Prof. Dr. D. Voiry
Institut Européen des Membranes, IEM, UMR 5635, Université Montpellier, ENSCM, CNRS
34000 Montpellier (France)
[+] These authors contributed equally to this work.

ments achieved through diatomic catalysts to manipulate the coordination structure and charge distribution to enhance catalytic activity,[10] the fundamental limitations persist.

It is well known that the coordination structure of thesingle atom site (such as the first shell coordination structure, coordination number, bond length, etc.) funda- mentally influences the adsorption characteristics of intermediates.[5a,11] Therefore, a promising strategy is to design SACs that automatically regulate the coordination number or bond length during CO_2RR.[12] In this work, we engineered an asymmetric coordination SAC with an atom- dispersed Fe S_1N_3 coordination structure. The presence of sulfur atoms with a large geometric radius causes significant geometric distortion in the Fe—S_1N_3 sites by protruding from the first shell coordination plane. Furthermore, the Fe S_1N_3 exhibits distinctive self-relaxation behavior in response to different adsorption intermediates during the electrochemical CO_2RR process. The dynamic change in bond length optimizes the charge transfer between the Fe sites and intermediates independently, thereby lowering the energy barrier of CO_2RR. The developed Fe S_1N_3 catalyst exhibits exceptional performance with a considerable CO Faradaic efficiency (FE_{CO}) of 99.02 % at 0.50 V (versus RHE) and remarkable stability. Our work presents a valuable strategy for designing high performance electrochemical CO_2RR catalysts.

Results and Discussion

We demonstrated an asymmetric coordination Fe-Based SAC with a geometric distortion that exhibits adaptive relaxation ability during the electrochemical CO_2RR process shown in Figure 1A. Using a modified continuous two-step approach, we prepared a series of Fe-Based monatomic catalysts with various geometric distortions. At the first step, we prepared a ZIF-8 precursor with a uniform rhombic dodecahedral structure (Figure S1). By annealing the ZIF-8 precursor, we successfully obtained an N-doped carbon carrier (NC) (Figure S2), as confirmed by X-ray diffraction (XRD) patterns showing the destruction of the crystal structure of ZIF-8 and the formation of a carbon substrate (Figure S3).[11c,13] Next, we immersed NC in a $Fe(acacac)_3$ solution to decorate Fe ions, which were then annealed with melamine, sublimed sulfur and boric acid to from Fe—N_4, Fe S_1N_3 and Fe B_1N_3, respectively (details are provided in the Supporting Information). Scanning electron microscopy (SEM) and transmission electron microscopy (TEM) images revealed that the rhombic dodecahedron morphology was well preserved, although the surface appeared slightly collapsed (Figure 1B, Figure S4 and S5). The Fe content measured via inductively coupled plasma-atomic emission spectrometry (ICP-AES) was found to be 1.03 wt% for Fe N_4, 1.03 wt% for Fe S_1N_3, and 1.07 wt% for Fe B_1N_3 (Table S1). Notably, no bulk-like metallic phases were observed in the high-resolution TEM (HR-TEM) and XRD analyses, indicating the absence of metal atom agglomeration (Figure S6).[14] Additionally, Brunauer–Emmett–Teller (BET) analysis confirmed the porous nanostructures of Fe—N_4, Fe—S_1N_3, and Fe—B_1N_3, which provide enhanced surface area and more channels for electrolyte and CO_2 accessibility (Figure S7). Furthermore, Raman spectra showed a higher degree of graphitization for the Fe—N_4, Fe S_1N_3 and Fe B_1N_3 than NC (Figure S8), suggesting that the carbon vacancies were repaired by anchoring Fe atoms.[15]

The catalyst atomic structures were examined using aberration-corrected high-angle annular dark-field scanning transmission electron microscopy (HAADF-STEM). Fig-ure 1C illustrates that bright spots are randomly dispersed on Fe S_1N_3, without metal clusters or particles. Electron energy loss spectroscopy (EELS) analysis in Figure 1D confirms that these bright spots correspond to Fe atoms coordinated with S and N atoms. The element mappingfurther reveals the uniform distribution of Fe, C, and N throughout the entire nanostructure in Fe—N_4, Fe—S_1N_3, and Fe B_1N_3 (Figure 1E–1I, Figure S9, and Figure S10). It also can be seen that S and B atoms were introduced into Fe S_1N_3 and Fe B_1N_3, respectively.

The X-ray photoelectron spectroscopy (XPS) analysis was conducted to characterize the chemical states and elemental composition of catalysts. The high-resolution Fe 2p spectra (Figure 2A) confirm the anchoring of Fe atoms on the three catalysts. Interestingly, the oxidation states of Fe were found to raise with increasing electro- negativity of the first shell coordination heteroatoms. TheC N, C S, and C B bond signals were observed in the C 1s spectra of Fe N_4, Fe S_1N_3, and Fe B_1N_3 (Figure S11A),[16] which corresponded to N 1s, S 2p, and B 1s spectra (Fig- ure S11B and S12), further indicating the incorporation of Sand B atoms into Fe S_1N_3 and Fe B_1N_3, respectively. InN 1s spectra, the peaks at 399.4 eV are attributed to metal-N ($M—N_x$) bonds.[17] Notably, Fe—S, and Fe—B bond were observed in Fe—S_1N_3 and Fe—B_1N_3, respectively, indicating the coordination of Fe atoms through Fe—N_α, Fe—$S_\beta N_\gamma$, and Fe $B_\delta N_\varepsilon$ bond in Fe N_4, Fe S_1N_3, and Fe B_1N_3, respec- tively. To gain insights into the precise electronic structure and local coordination environments, X-ray absorption fine-structure (XAFS) analysis was performed. The Fe K-edge XANES spectra of Fe N_4, Fe S_1N_3 and Fe B_1N_3 displayed absorption energies between those of Iron phthalocyanine (FePc, II) and Fe_2O_3 (Figure 2B), suggesting that the oxidation state of Fe in catalysts fall between Fe^{2+} and Fe^{3+}. The Fe oxidation state from high to low follows the order of Fe N_4 > Fe S_1N_3 > Fe B_1N_3, consistent with the XPS results. Fourier transformed (FT)-EXAFS spectra revealed signifi- cant differences in the local coordination of the Fe sites among the catalysts. Specifically, the Fe K-edge FT-EXAFS spectra of FePc and Fe—N_4 exhibited a main peak at ~1.47 Å, corresponding to the Fe—N path.[18] This peak shifted to ~1.66 Å and ~1.55 Å in Fe S_1N_3 and Fe B_1N_3, respectively, indicating changes in the first shell coordination environment due to the incorporated S and B atoms.[16b,19] Notably, no Fe Fe bond was observed in the three catalysts. Wavelet transform (WT)-EXAFS analysis of the Fe K-edge further supported the single-atom dispersion of Fe in Fe N_4, Fe S_1N_3, and Fe B_1N_3 (Figure 2D). The WT-EXAFS contour plots exhibited maximum peaks at

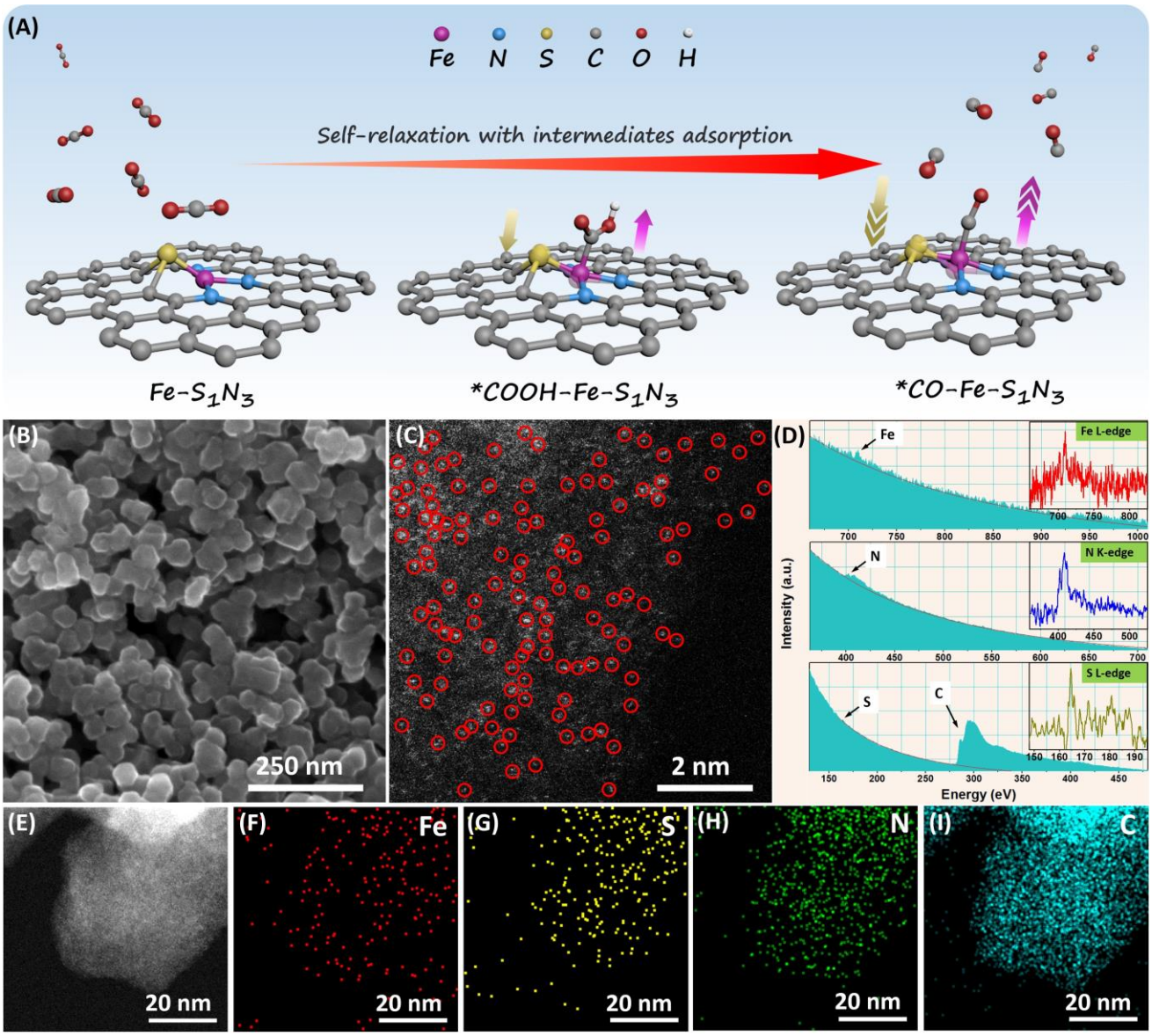

Figure 1. (A) Illustration showcasing the structural distortion of the Fe—S_1N_3 site with adsorbed various intermediates. (B) Scanning electron microscopy (SEM) image displaying the morphology of Fe—S_1N_3. (C) Aberration-corrected high-angle annular dark-field scanning transmission electron microscopy (HAADF-STEM) image, with some Fe atoms highlighted by red circles. (D) Electronic energy loss spectroscopy (EELS) analysis of Fe—S_1N_3. (E)–(I) HAADF-STEM images of Fe—S_1N_3 combined with energy-dispersive X-ray spectroscopy (EDX) mappings of individual elements, including Fe, S, N, and C.

$\pm$4.7 $Å^{-1}$, representing the Fe—N, Fe—S, and Fe—B contributions. However, compared with the WT-EXAFS signals of Fe foil, the presence of a Fe—Fe path (7.0 $Å^{-1}$) was not observed in the three catalysts, consistent with the HAADF-STEM results, further providing the single-atom dispersion of Fe.

Based on the analysis of X-ray absorption fine-structure (XAFS) data and quantitative least-squares EXAFS curve fittings, the coordination configurations of Fe-Based SACs were characterized. The Fe—N_4 catalyst shows a coordination number (C.N.) of approximately 4, with only Fe—N bonds present. The bond length of Fe—N in Fe—N_4 was measured to be 2.01 $\pm$ 0.01 Å (Figure 2E, S13 and Table S2). The Fe—S_1N_3 and Fe—B_1N_3 catalysts also contained Fe—N bonds, but with a C.N of $\pm$3. Additionally, Fe—S_1N_3 catalysts possessed Fe—S bonds, while the Fe—B_1N_3 catalyst had Fe—B bonds, both with a C.N. of $\pm$1 (Figure 2F–2G). We also found a longer bond length of Fe—S in Fe—S_1N_3 (2.23 $\pm$ 0.01 Å) compared to that of Fe—N in Fe—N_4 (2.01 $\pm$ 0.01 Å), while the bond length of Fe—N in Fe—S_1N_3 (1.94 $\pm$ 0.01 Å) was shorter than that of Fe—N in Fe—N_4. This difference in bond lengths is attributed to the larger geometric radius of the S atoms causing a significant geometric distortion in the Fe—S_1N_3 sites. In contrast, the smaller geometric distortion in Fe—B_1N_3 suggests that the protrusion of Fe atoms from the plane is responsible for both Fe—B and Fe—N bonds

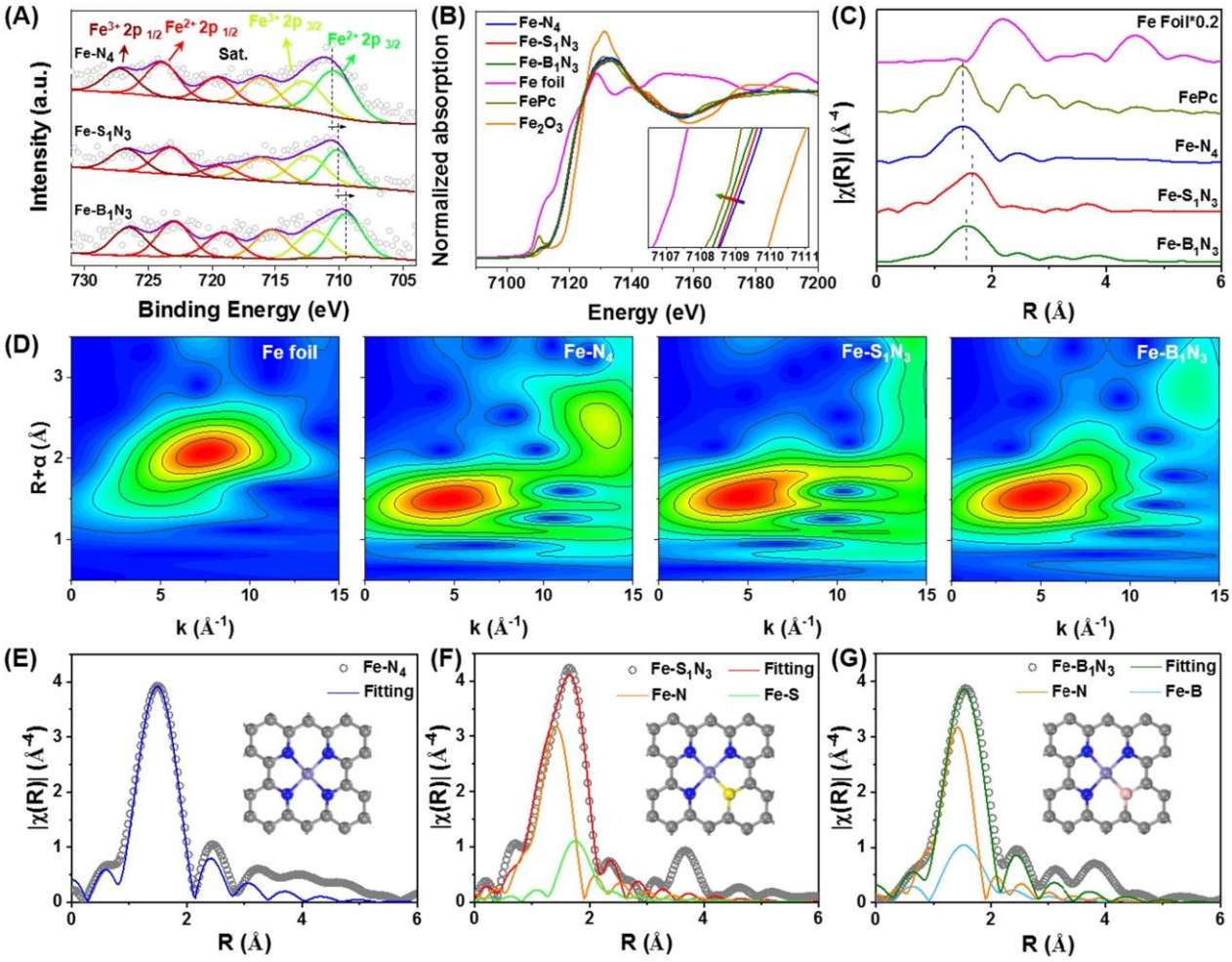

Figure 2. (A) High-resolution Fe 2p spectrum of Fe—N_4, Fe—S_1N_3, and Fe—B_1N_3. (B) The normalized Fe *K*-edge XANES spectra of Fe Foil, Fe_2O_3, FePc, Fe—N_4, Fe—S_1N_3 and Fe—B_1N_3. The inset shows the enlarged spectra. (C) Fourier-transform EXAFS spectra at Fe *K*-edge. (D) Wavelet transform EXAFS of k^3-weighted *k*-space spectra of different samples. Fe *K*-edge EXAFS fitting curves of Fe—N_4 (E), Fe—S_1N_3 (F) and Fe—B_1N_3 (G).

being longer than the Fe_N bonds in Fe_N_4. The structural models depicted in Figure 2E–2G were used for EXAFS curve fitting and supported the experimental spectra. Based on these observations, it is suggested the Fe_S_1N_3 structure consists of a Fe atom with three coordination N atoms and one protruding S atom. Similarly, the Fe_B_1N_3 structure consists of a slightly protruding Fe atom with three coordination N atoms and one B atom. The in-plane Fe_N_4 structure comprises one Fe atom and four coordinated N atoms.

The electrochemical activities of the Fe-Based catalysts for CO_2RR were evaluated using linear sweep voltammetry (LSV). Figure 3A shows that Fe—S_1N_3 catalyst exhibits a higher current density than Fe_N_4 and Fe_B_1N_3 catalysts, indicating its superior electrochemical activity. A control experiment further confirmed this, where the Fe—S_1N_3 catalyst showed higher current density in CO_2-saturated electrolyte compared to Ar-saturated electrolyte (Fig-ure S14).[20] The reduction products were analyzed using hydrogen nuclear magnetic resonance (^{1}H NMR) spectroscopy and on-line gas chromatography (GC). The results reveal that only CO and H_2 were detected as the products (Figure 3B and Figure S15–S16). Importantly, Fe—S_1N_3 achieved an exceptional selectivity (maximum FE_{CO} of 99.02 % at —0.50 V), higher than Fe—N_4 (91.53 %) andFe—B_1N_3 (90.17 %). Meanwhile, Fe—S_1N_3 exhibited a re- markable FE_{CO} above 90 % across a wide potential range of —0.40 to —1.10 V. The intrinsic activities of the three catalysts were further compared using j_{CO} and turnover frequency (TOF) (Figure 3C and 3D). The Fe—S_1N_3 exhibitsa satisfactory j_{CO} (—77.15 ±4.46 mAcm^{-2}), which was higher that of Fe—N_4 (—24.58 ±0.33 mAcm^{-2}) and Fe—B_1N_3(11.93 0.47 mAcm^{-2}). Fe_S_1N_3 catalyst demonstrates an impressive TOF value of approximately 7804.34 h^{-1}, surpass-ing Fe_N_4 (2486.94 h^{-1}) and Fe_B_1N_3 (1306.86 h^{-1}) by 214 % and 547 %, respectively. It was also found that the performance of the three catalysts displayed the same trend in the H-type cell (Figure S17–S18). Meanwhile, the single pass carbon efficiency (SPCE) and energy efficiency (EE) was also determined to estimate the potential scalability of the

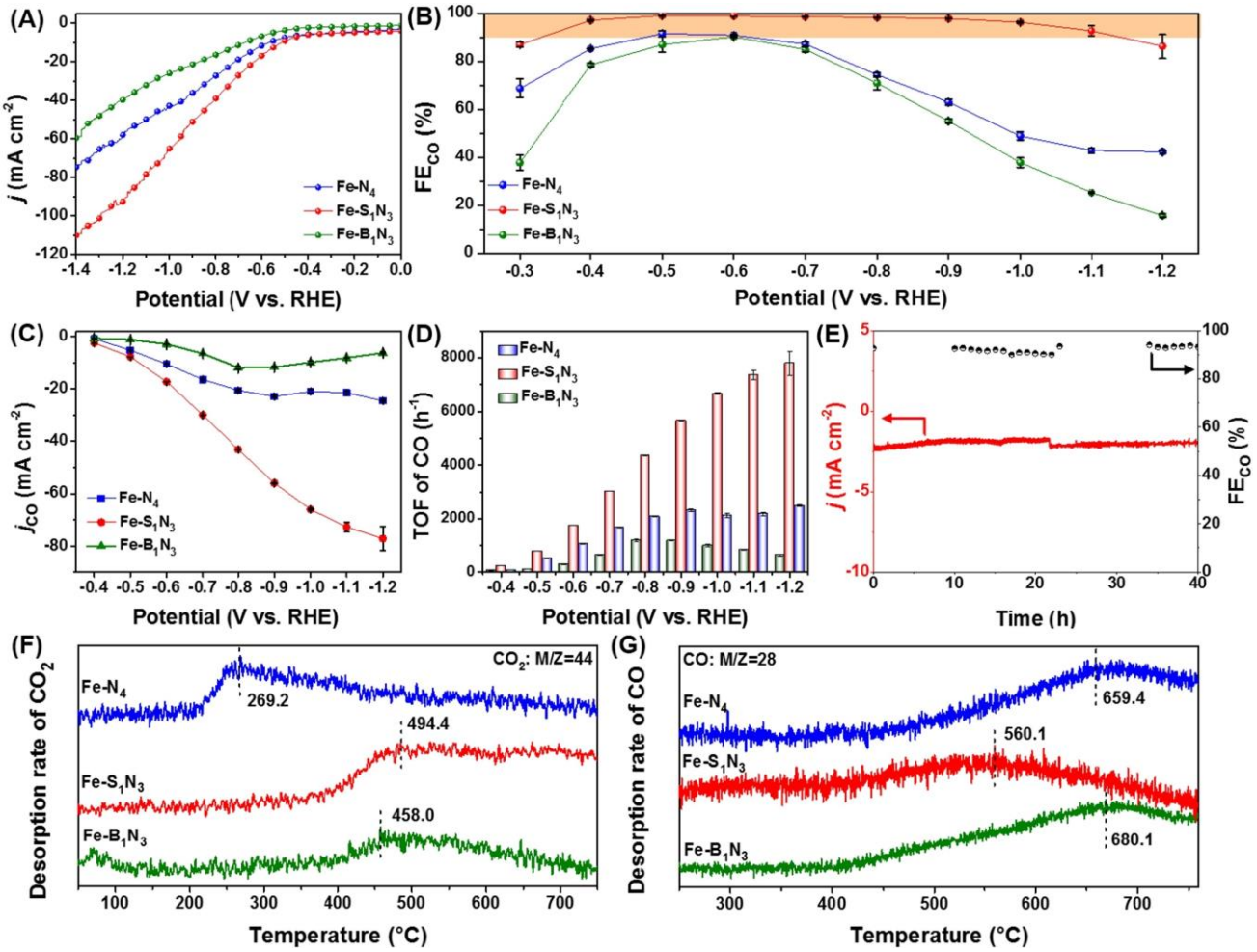

Figure 3. Electrocatalytic performance in the flow cell: (A) LSV curves recorded in CO_2-saturated $KHCO_3$ electrolyte. (B) Faradaic efficiency (FE) for CO production at specific potentials. (C) CO partial current density of the prepared catalysts at specific potentials. (D) TOFs for CO production at specific potentials. (E) Long-term stability evaluation of Fe—S_1N_3 catalysts at —0.50 V potential in H-type cell. CO_2 (F) and CO (G) temperature-programmed desorption profiles of Fe—N_4, Fe—S_1N_3, and Fe—B_1N_3.

catalysts in CO_2RR system (Figure S19). It could be observed that the Fe_S_1N_3 catalyst presented a higher value of SPCE and EE than those of any other samples at all applied potentials. These findings indicate that the Fe_S_1N_3 catalyst significantly improves the selectivity and intrinsic activity for electrochemical CO_2RR compared to Fe—N_4 and Fe—B_1N_3.

The metal content dependent electrocatalytic CO_2 reduction performance of Fe_S_1N_3 catalysts were investigated using XRD, SEM and electrochemical analysis (Figure S20–S22). It can be seen that the catalytic activity and selectivity initially increased and then decreased with increasing Fe content. This trend can be attributed to the fact that an initial increase in Fe atoms improves the density of active sites on Fe_S_1N_3. However, excessive Fe leads to the formation of FeS, which degrades the catalytic activity. Additionally, Figure S23–S26 reveal that the nitrogen-doped carbon (NC) and sulfur-doped nitrogen-carbon (S_NC) substrates slightly contribute to the catalytic activity, as shown by their low selectivity and negligible j_{CO}. These results further emphasize the superior performance of the Fe_S_1N_3 site.

The stability is another crucial factor in catalyst evaluation. The chronoamperometry measurements (Figure 3E) demonstrated that the FE_{CO} current density of the Fe_S_1N_3 catalyst remained relatively stable after a 40-hour continuous operation. Similarly, both Fe_N_4 and Fe_B_1N_3 catalysts displayed favorable electrochemical stability (Figure S27). Morphological analysis, oxidation state analysis, and crystallinity characterization (Figure S28) indicated no significant changes in the Fe_S_1N_3 catalyst after potentiostatic electrolysis. EDS mapping (Figure S29) confirmed that the C, N, S and Fe elements were still uniformly distributed on Fe_S_1N_3, further highlighting its outstanding stability.

To understand the origin of the improved performances, we conducted CO_2 and CO temperature-programmed desorption (TPD) analysis. Figure 3F shows TPD signal peaks of CO_2 desorption at 269.2 °C, 494.4 °C and 458.0 °C on Fe—N_4, Fe—S_1N_3 and Fe—B_1N_3, respectively. The highest desorption temperature of CO_2 on Fe—S_1N_3 indicates its

strong CO_2 adsorption capacity. Figure 3G illustrates the CO TPD spectrums of Fe N_4, Fe S_1N_3 and Fe B_1N_3, corresponding to the adsorption of *CO intermediates at the active site.[13,16a] The results reveal that the CO TPD signal peak of Fe—S_1N_3 is located at 560.1 °C, lower than that of Fe N_4 (659.4 °C) and Fe B_1N_3 (680.1 °C), suggesting a facilitated desorption step of the *CO intermediates on Fe—S_1N_3. Taken all together, our results indicate that the stronger CO_2 adsorption and easier CO desorption capacity of Fe S_1N_3 may be the key factors for the improvement of catalytic activity.

DFT calculations were performed to investigate internal factors responsible for breaking the linear scaling relationship in the electrochemical CO_2RR process, leading to an improved intrinsic activity. FeN_4, Fe_S_1N_3, and Fe_B_1N_3 models were constructed and validated by EXAFS fitting results (Figure S30) and matched well with experimentally-determined Fe_N_4, Fe_S_1N_3, and Fe_B_1N_3 structures. The asymmetric coordination environment and large geometric distortion result in an asymmetric distribution of the lowest unoccupied molecular orbital (LUMO) at Fe_S_1N_3 sites (Figure S31). A better symmetry match was observed between the highest occupied molecular orbital (HOMO) of CO_2 and the LUMO of Fe—S_1N_3, facilitating the adsorption and activation of CO_2 on the Fe—S_1N_3 site.[5a,21] Furthermore, it was found that Fe_S_1N_3 exhibits the highest CO_2 adsorption energy (Figure S32) and lowest *COOH formation energy (Figure 4A), further confirming the superiority of the Fe—S_1N_3 structure in the adsorption and activation of CO_2 molecules. Figure 4B shows that the Fe_S_1N_3 site could provide the most electrons for the *COOH intermediate than other active sites, with the least electron transfer between Fe—S_1N_3 and *CO intermediates, resulting in the Fe—S_1N_3 site exhibiting the highest *COOH adsorption energy among all active sites, promoting CO_2 activation and *COOH formation. Simultaneously, the Fe_S_1N_3 active site displays the lowest *CO adsorption energy and facilitates *CO desorption. Our DFT results gain an in-depth understanding of the mechanism that the Fe—S_1N_3 site effectively reduces the free energy of electrocatalytic CO_2RR by breaking the linear scaling relationships, consistent with experimental observations.

To investigate the atomic-scale origin of the catalytic activity enhancement, we initially focused on the effect of electronegativity of the coordination heteroatoms on electron transfer between active sites and intermediates (Figure S33). It was found that the electronegativity of coordination heteroatoms and the oxidation state of Fe was not correlated with the electron transfer or intermediate adsorption energy, indicating that electronegativity is not a critical factor in influencing catalytic behavior. Furthermore, the CO_2 adsorption energy on Fe atom at Fe—S_1N_3 site (—0.21 eV) is much greater than that of S atom at Fe—S_1N_3 site (–0.06 eV), and the optimized model shows that CO_2 is difficult to be stably adsorbed at the S site and is more likely to be adsorbed and activated at the Fe site (Figure S34). These evidences indicate that the S atom on Fe_S_1N_3 site is inert, although its an electron donor. Notably, both Fe and S in Fe—S_1N_3 site are electron donors, resulting in a repulsive force between the Fe and S atoms, which may be the reason for the shorter Fe N bond length in Fe S_1N_3. We thenfocused on the bond length of the active site and its operando evolution, which may be the underlying cause of the varying electron transfer capability.[22] It was observed that the Fe S_1N_3 site, with significant geometric distortion, exhibits a noticeable self-relaxation during the electrochem- ical CO_2RR process (Figure 3C and Table S3). Specifically, the Fe S_1N_3 site releases adsorption intermediates depend- ent strain, resulting in variations in bond length. On the other hand, the structure of the Fe B_1N_3 site displays a weakly dynamic evolution (Figure S35). In contrast, theFe N_4 site with a symmetrical coordination structure shows a negligible deformation during the electrocatalytic process (Figure S36), likely due to the Fe atoms not protruding fromthe basal plane. The bond length analysis also reveals the structure-performance relationship at different active sites. The refinement of the geometric coordination environment around the Fe site, triggered by strain release, inevitably affects the interaction between the active site and the adsorbed intermediate.[11b,22b] Among the three catalysts, the Fe—S_1N_3 exhibited the largest average bond length between Fe and coordination atom, while the Fe_N_4 had the smallest average bond length. This observation is attributed to different degrees of geometric distortion. Furthermore, as the average bond length increased, the electron transfer and interaction between the Fe sites and the *COOH intermediates were enhanced (Figure 4D). It was found that sizeable geometric distortion and considerable bond length lead to an accumulation of electrons at Fe sites, promoting intermediates adsorption and electron transfer (Figure S37).[23] Similarly, the electron transfer and interactions between the Fe sites and the *CO intermediate initially increase with the bond length increase (Figure 4E). However, as the bond length further increased, the electron transfer decreased.This is because an excessively long bond length between theFe atom and the coordination atom weakens the originalFe S/Fe N interaction and reduces the electron transfer from S and N atoms to adsorbed *CO via the shared Fe atom.[11b] These findings suggest that the dynamic evolutionof the Fe S_1N_3 structure during the catalytic process enables the independent regulation of the *COOH intermediate and *CO intermediate adsorption energies, thereby breaking the linear scaling relationships and enhancing intrinsic activity.

To get further understanding of the dynamic behavior of catalyst, the operando behavior of the active sites on the three catalysts was characterized using in situ XAFS spectroscopy. This allowed us to obtain experimental evidence of the dynamic evolution of the geometric structure induced by the adsorbed intermediates. The Fe *K*-edge in situ XANES spectra were collected for the different catalysts in a CO_2-saturated 0.1 M $KHCO_3$ solutionunder open-circuit potential (OCP) and at 0.5 V (Fig- ure 5A). Comparing the spectra obtained under OCP with those at 0.5 V, we observed a blue shift in the adsorption edge for all three catalysts indicating an elevated Fe oxidation state, which can be attributed to the electron transfer from the Fe site to adsorbed intermediates.[24] This suggests that the intermediates are thermodynamically

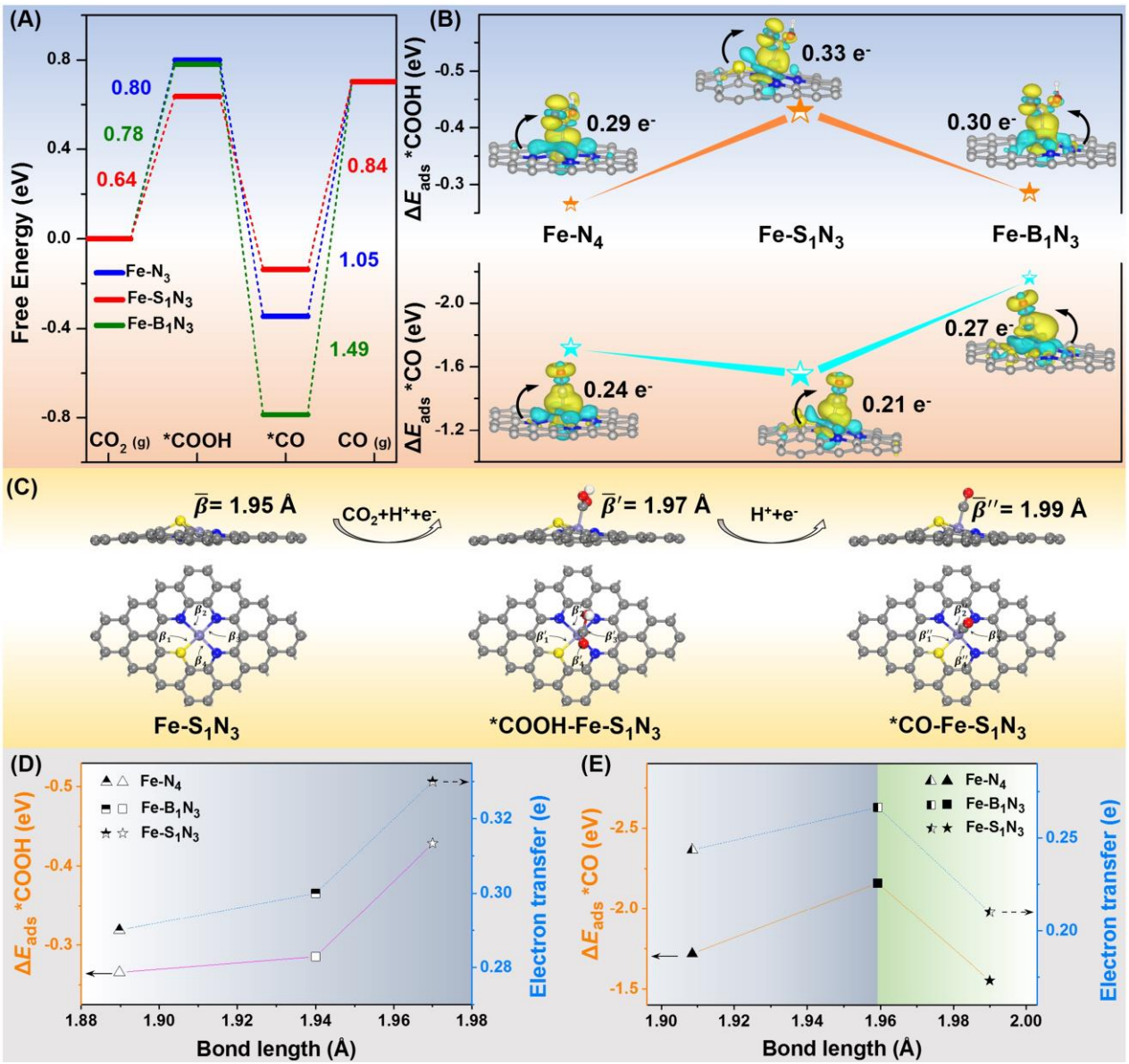

Figure 4. (A) Free energy diagrams illustrating the catalytic performance of different catalysts in CO_2RR. (B) Absorption energy of *COOH intermediates and *CO intermediates on various catalytic sites. (C) Dynamic evolution and average bond length changes of Fe—S_1N_3 sites during the CO_2RR process. (D) Average bond length, charge transfer of *CO—Fe site, and *CO intermediate adsorption energy of different sites in the CO_2RR process. (E) Average bond length, charge transfer of *COOH—Fe site, and *COOH intermediate adsorption energy on different sites in the CO_2RR process.

favorable to adsorb on Fe atoms, in good agreement with our DFT calculations. Furthermore, in situ EXAFS spectroscopy was performed to monitor the dynamic evolution of active sites structures during electrochemical CO_2RR (Figure 5B–D). The Fe *K*-edge FT-EXAFS spectra of Fe—N_4 under OCP displayed a peak at ~1.44 Å, corresponding to the Fe—N bond. The peak of Fe S_1N_3 and Fe B_1N_3 show distinct blue shifts, attributed to the presence of S and B atoms, respectively, consistent with the results obtained from ex situ measurements (Figure 2). The in situ FT-EXAFS curves robustly exhibit the dominant peak corresponding to the Fe—N bond, suggesting no agglomeration of metal atoms or bond breakage.[12,25] However, the prominent peak of the Fe—S_1N_3 site shows a pronounced blue shift compared to the Fe—B_1N_3 site, while the change in the Fe—N_4 site was negligible (Figure 5E). This confirms that the bond length at the Fe S_1N_3 site undergoes the most pronounced dynamic evolution during the electrochemical CO_2RR process, consistent with our DFT calculations. In summary, our in situ spectroscopy study provides insights into the bond length and atomic structure evolution of the Fe N_4, Fe S_1N_3, and Fe B_1N_3. The dynamic evolution of bond length via strain relaxation may contribute to

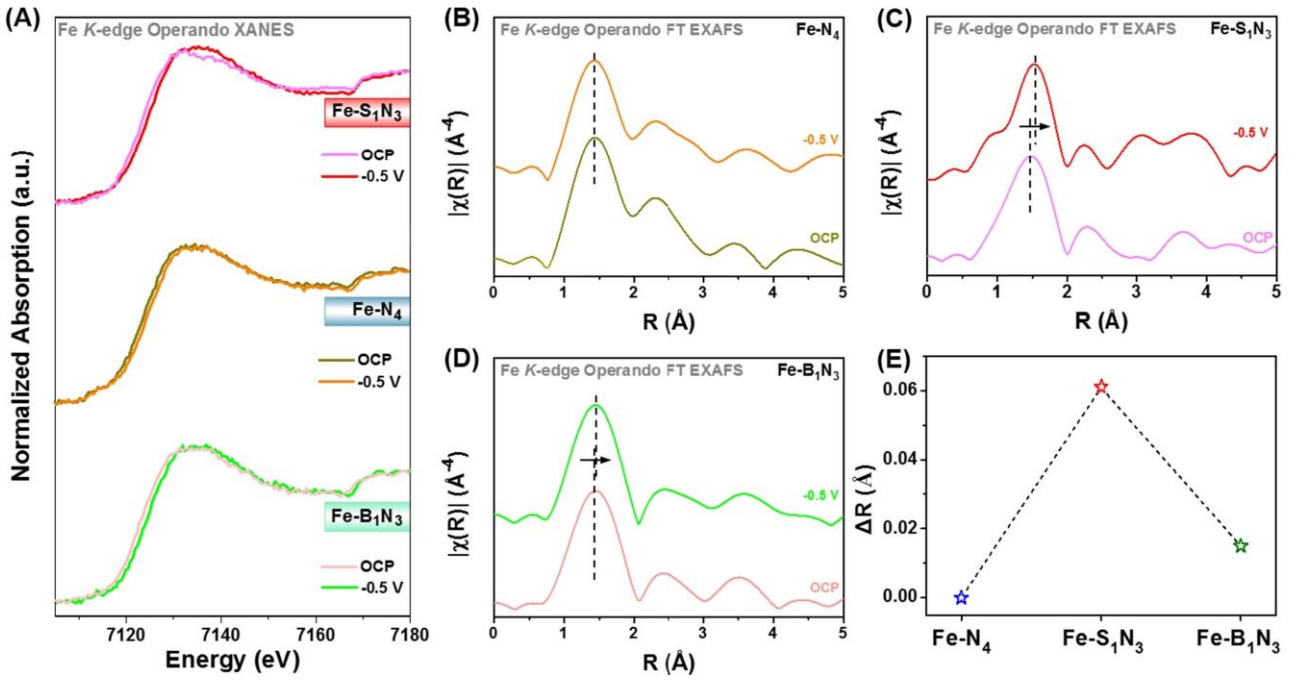

Figure 5. (A) Operando Fe *K*-edge XANES spectra of Fe—N_4 Fe—S_1N_3 and Fe—B_1N_3. k^3-weighted FT-EXAFS of the Fe *K*-edge for Fe—N_4(B), Fe—S_1N_3 (C), and Fe—B_1N_3 (D) under different applied potentials of OCP and —0.5 V. (E) The change in bond lengths of Fe—N_4, Fe—S_1N_3, and Fe—B_1N_3 obtained from the operando *R*-space EXAFS spectrum.

enhanced CO_2RR activity as supported by our numerical simulation results.

Conclusion

To summarize, we have developed an asymmetric coordination Fe single atom catalyst, denoted as Fe–S_1N_3, consisting of Fe atoms coordinated with one S atom and three N atoms. The Fe S_1N_3 catalyst exhibits a remarkable CO_2RR intrinsic activity, with a maximum TOF of 7804.34 h^{-1}, and an excellent selectivity, achieving a FE_{CO} of 99.02% at –0.50 V. Importantly, our catalyst breaks the linear scaling relationships, enabling enhance catalytic performance. The combination of the ex situ/operando XAFS spectra analysis and DFT calculations reveals that the larger size of the S atom induces significant geometric distortion in Fe—S_1N_3 sites. As a result, the Fe–S_1N_3 sites display adaptive relaxation through strain release during the adsorption of different intermediates. Notably, the dynamic evolution of the bond length during the catalytic process allows for independent modulation of the adsorption energies of *COOH intermediate and *CO intermediate. This capability further disrupts the linear scaling relationship and improves the intrinsic activity of the catalyst. This research provides valuable insights into the rational design and precise modulation of targeted catalysts via precise engineering of the active site. At the atomic scale, it enhances our understanding of the structure–activity relationships in electrochemical CO_2RR. The findings presented here shed light on developing highly efficient and selective catalysts, contributing to the advancement of CO_2 conversion technologies.

Supporting Information

The authors have cited additional references within the Supporting Information.[26]

Acknowledgements

The authors gratefully acknowledge the financial support provided by the National Natural Science Foundation of China (grand numbers 22279044 and 12034002), the Project for Self-Innovation Capability Construction of Jilin Province Development and Reform Commission (2021C026), Jilin Province Science and Technology Development Program (20210301009GX), and the Fundamental Research Funds for the Central Universities. The authors also acknowledge the facilities and computing resources provided by LvLiang Cloud Computing Center of China. The computational calculations were performed on the TianHe-2 supercomputer.

Conflict of Interest

The authors declare no conflict of interest.

Data Availability Statement

The data that support the findings of this study are available in the supplementary material of this article.

Keywords: Asymmetric Coordination · CO_2 Reduction Reaction · Dynamic Evolution · Self-Relaxation · Single Atom Catalysts

[1] a) Y. Yang, S. Louisia, S. Yu, J. Jin, I. Roh, C. Chen, M. V. Fonseca Guzman, J. Feijóo, P.-C. Chen, H. Wang, C. J. Pollock, X. Huang, Y.-T. Shao, C. Wang, D. A. Muller, H. D. Abruña, P. Yang, *Nature* **2023**, *614*, 262–269; b) R. Amirbei- giarab, J. Tian, A. Herzog, C. Qiu, A. Bergmann, B. Roldan Cuenya, O. M. Magnussen, *Nat. Catal.* **2023**, *6*, 837–846; c) C. Chen, X. Yan, Y. Wu, S. Liu, X. Zhang, X. Sun, Q. Zhu, H. Wu, B. Han, *Angew. Chem. Int. Ed.* **2022**, *61*, e202202607; d) H. Zhang, J. Gao, D. Raciti, A. S. Hall, *Nat. Catal.* **2023**, *6*, 807–817; e) S. Liang, J. Xiao, T. Zhang, Y.Zheng, Q. Wang, B. Liu, *Angew. Chem. Int. Ed.* **2023**, *62*, e202310740.

[2] a) K. M. Lee, J. H. Jang, M. Balamurugan, J. E. Kim, Y. I. Jo, K. T. Nam, *Nat. Energy* **2021**, *6*, 733–741; b) M. Zhong, K.Tran, Y. Min, C. Wang, Z. Wang, C.-T. Dinh, P. De Luna, Z. Yu, A. S. Rasouli, P. Brodersen, S. Sun, O. Voznyy, C.-S. Tan, M. Askerka, F. Che, M. Liu, A. Seifitokaldani, Y. Pang, S.-C. Lo, A. Ip, Z. Ulissi, E. H. Sargent, *Nature* **2020**, *581*, 178–183; c) J. Yin, J. Jin, Z. Yin, L. Zhu, X. Du, Y. Peng, P. Xi, C.-H. Yan, S. Sun, *Nat. Commun.* **2023**, *14*, 1724; d) D. Chen, L.-H. Zhang, J. Du, H. Wang, J. Guo, J. Zhan, F. Li, F. Yu, *Angew. Chem. Int. Ed.* **2021**, *60*, 24022–24027; e) T. Wang, J. Chen, X. Ren, J. Zhang, J. Ding, Y. Liu, K. H. Lim, J. Wang, X. Li, H. Yang, Y. Huang, S. Kawi, B. Liu, *Angew. Chem. Int. Ed.* **2023**, *62*, e202211174.

[3] a) J. Zhang, C. Guo, S. Fang, X. Zhao, L. Li, H. Jiang, Z. Liu, Z. Fan, W. Xu, J. Xiao, M. Zhong, *Nat. Commun.* **2023**, *14*, 1298; b) F. Yu, J. Zhan, D. Chen, J. Guo, S. Zhang, L.-H. Zhang, *Adv. Funct. Mater.* **2023**, *33*, 2214425; c) C. Wang, X. Wang, H. Ren, Y. Zhang, X. Zhou, J. Wang, Q. Guan, Y. Liu, W. Li, *Nat. Commun.* **2023**, *14*, 5108.

[4] a) L. Ju, X. Tan, X. Mao, Y. Gu, S. Smith, A. Du, Z. Chen, C. Chen, L. Kou, *Nat. Commun.* **2021**, *12*, 5128; b) Y. Dai, H. Li, C. Wang, W. Xue, M. Zhang, D. Zhao, J. Xue, J. Li, L. Luo, C. Liu, X. Li, P. Cui, Q. Jiang, T. Zheng, S. Gu, Y. Zhang, J. Xiao, C. Xia, J. Zeng, *Nat. Commun.* **2023**, *14*, 3382; c) S. Wang, L. Wang, D. Wang, Y. Li, *Energy Environ. Sci.* **2023**, *16*, 2759–2803; d) B. Singh, M. B. Gawande, A. D. Kute, R. S. Varma, P. Fornasiero, P. McNeice, R. V. Jagadeesh, M. Beller,R. Zbořil, *Chem. Rev.* **2021**, *121*, 13620–13697.

[5] a) Y. Wang, G. Jia, X. Cui, X. Zhao, Q. Zhang, L. Gu, L. Zheng, L. H. Li, Q. Wu, D. J. Singh, D. Matsumura, T. Tsuji, Y.-T. Cui, J. Zhao, W. Zheng, *Chem* **2021**, *7*, 436–449; b) J. Pei, L. Yang, J. Lin, Z. Zhang, Z. Sun, D. Wang, W. Chen, *Angew. Chem. Int. Ed.* **2024**, *63*, e202316123; c) J. Hulva, M. Meier, R. Bliem, Z. Jakub, F. Kraushofer, M. Schmid, U. Diebold, C. Franchini, G. S. Parkinson, *Science* **2021**, *371*, 375–379.

[6] a) F. Pan, Y. Yang, *Energy Environ. Sci.* **2020**, *13*, 2275–2309; b) J. H. Kim, H. Jang, G. Bak, W. Choi, H. Yun, E. Lee, D. Kim, J. Kim, S. Y. Lee, Y. J. Hwang, *Energy Environ. Sci.* **2022**, *15*, 4301–4312; c) W. Ren, A. Xu, K. Chan, X. Hu, *Angew. Chem. Int. Ed.* **2022**, *61*, e202214173.

[7] a) W. Zhou, H. Su, W. Cheng, Y. Li, J. Jiang, M. Liu, F. Yu, W. Wang, S. Wei, Q. Liu, *Nat. Commun.* **2022**, *13*, 6414; b) Y. Wang, B. J. Park, V. K. Paidi, R. Huang, Y. Lee, K.-J. Noh, K.-S. Lee, J. W. Han, *ACS Energy Lett.* **2022**, *7*, 640–649.

[8] J. Gu, C.-S. Hsu, L. Bai, H. M. Chen, X. Hu, *Science* **2019**, *364*, 1091–1094.

[9] J. Gu, S. Liu, W. Ni, W. Ren, S. Haussener, X. Hu, *Nat. Catal.* **2022**, *5*, 268–276.

[10] a) J. Pei, T. Wang, R. Sui, X. Zhang, D. Zhou, F. Qin, X. Zhao, Q. Liu, W. Yan, J. Dong, L. Zheng, A. Li, J. Mao, W. Zhu, W. Chen, Z. Zhuang, *Energy Environ. Sci.* **2021**, *14*, 3019–3028; b) W. Ren, X. Tan, W. Yang, C. Jia, S. Xu, K. Wang, S. C. Smith, C. Zhao, *Angew. Chem. Int. Ed.* **2019**, *58*, 6972–6976; c) H. Cheng, X. Wu, M. Feng, X. Li, G. Lei, Z. Fan, D. Pan, F. Cui, G. He, *ACS Catal.* **2021**, *11*, 12673–12681.

[11] a) X. Wang, Z. Chen, X. Zhao, T. Yao, W. Chen, R. You, C. Zhao, G. Wu, J. Wang, W. Huang, J. Yang, X. Hong, S. Wei,Y. Wu, Y. Li, *Angew. Chem. Int. Ed.* **2018**, *57*, 1944–1948; b) G. Han, X. Zhang, W. Liu, Q. Zhang, Z. Wang, J. Cheng, T. Yao, L. Gu, C. Du, Y. Gao, G. Yin, *Nat. Commun.* **2021**, *12*, 6335; c) J. Guo, W. Zhang, L.-H. Zhang, D. Chen, J. Zhan, X. Wang, N. R. Shiju, F. Yu, *Adv. Sci.* **2021**, *8*, 2102884; d) D. Zhao, K. Yu, P. Song, W. Feng, B. Hu, W.-C. Cheong, Z. Zhuang, S. Liu, K. Sun, J. Zhang, C. Chen, *Energy Environ. Sci.* **2022**, *15*, 3795–3804.

[12] Z. Zhang, J. Zhu, S. Chen, W. Sun, D. Wang, *Angew. Chem. Int. Ed.* **2023**, *62*, e202215136.

[13] Z. Jin, M. Yang, Y. Dong, X. Ma, Y. Wang, J. Wu, J. Fan, D. Wang, R. Xi, X. Zhao, T. Xu, J. Zhao, L. Zhang, D. J. Singh, W. Zheng, X. Cui, *Nano-Micro Lett.* **2024**, *16*, 4.

[14] a) J. Zhu, M. Xiao, D. Ren, R. Gao, X. Liu, Z. Zhang, D. Luo, W. Xing, D. Su, A. Yu, Z. Chen, *J. Am. Chem. Soc.* **2022**, *144*, 9661–9671; b) L. Han, H. Cheng, W. Liu, H. Li, P. Ou, R. Lin, H.-T. Wang, C.-W. Pao, A. R. Head, C.-H. Wang, X. Tong, C.-J. Sun, W.-F. Pong, J. Luo, J.-C. Zheng, H. L. Xin, *Nat. Mater.* **2022**, *21*, 681–688.

[15] a) Y. Cao, L. Guo, M. Dan, D. E. Doronkin, C. Han, Z. Rao, Y. Liu, J. Meng, Z. Huang, K. Zheng, P. Chen, F. Dong, Y.Zhou, *Nat. Commun.* **2021**, *12*, 1675; b) J. Li, M. Chen, D. A. Cullen, S. Hwang, M. Wang, B. Li, K. Liu, S. Karakalos, M. Lucero, H. Zhang, C. Lei, H. Xu, G. E. Sterbinsky, Z. Feng, D. Su, K. L. More, G. Wang, Z. Wang, G. Wu, *Nat. Catal.* **2018**, *1*, 935–945.

[16] a) S. Chen, X. Li, C.-W. Kao, T. Luo, K. Chen, J. Fu, C. Ma, H. Li, M. Li, T.-S. Chan, M. Liu, *Angew. Chem. Int. Ed.* **2022**, *61*, e202206233; b) H. Shang, X. Zhou, J. Dong, A. Li, X. Zhao, Q. Liu, Y. Lin, J. Pei, Z. Li, Z. Jiang, D. Zhou, L. Zheng, Y.Wang, J. Zhou, Z. Yang, R. Cao, R. Sarangi, T. Sun, X. Yang, X. Zheng, W. Yan, Z. Zhuang, J. Li, W. Chen, D. Wang, J. Zhang, Y. Li, *Nat. Commun.* **2020**, *11*, 3049.

[17] Z. Zeng, L. Y. Gan, H. Bin Yang, X. Su, J. Gao, W. Liu, H. Matsumoto, J. Gong, J. Zhang, W. Cai, Z. Zhang, Y. Yan, B. Liu, P. Chen, *Nat. Commun.* **2021**, *12*, 4088.

[18] G. Yang, J. Zhu, P. Yuan, Y. Hu, G. Qu, B.-A. Lu, X. Xue, H. Yin, W. Cheng, J. Cheng, W. Xu, J. Li, J. Hu, S. Mu, J.-N. Zhang, *Nat. Commun.* **2021**, *12*, 1734.

[19] M. Wang, W. Yang, X. Li, Y. Xu, L. Zheng, C. Su, B. Liu, *ACS Energy Lett.* **2021**, *6*, 379–386.

[20] Y. Zhang, L.-Z. Dong, S. Li, X. Huang, J.-N. Chang, J.-H. Wang, J. Zhou, S.-L. Li, Y.-Q. Lan, *Nat. Commun.* **2021**, *12*, 6390.

[21] J. Li, S. Chen, F. Quan, G. Zhan, F. Jia, Z. Ai, L. Zhang, *Chem* **2020**, *6*, 885–901.

[22] a) H. Xu, D. Rebollar, H. He, L. Chong, Y. Liu, C. Liu, C.-J. Sun, T. Li, J. V. Muntean, R. E. Winans, D.-J. Liu, T. Xu, *Nat. Energy* **2020**, *5*, 623–632; b) X. Su, Z. Jiang, J. Zhou, H. Liu, D. Zhou, H. Shang, X. Ni, Z. Peng, F. Yang, W. Chen, Z. Qi, D. Wang, Y. Wang, *Nat. Commun.* **2022**, *13*, 1322.

[23] Q. Wang, K. Liu, K. Hu, C. Cai, H. Li, H. Li, M. Herran, Y.-R. Lu, T.-S. Chan, C. Ma, J. Fu, S. Zhang, Y. Liang, E. Cortés, M. Liu, *Nat. Commun.* **2022**, *13*, 6082.

[24] a) N. Zhang, T. Zhou, J. Ge, Y. Lin, Z. Du, C. a. Zhong, W. Wang, Q. Jiao, R. Yuan, Y. Tian, W. Chu, C. Wu, Y. Xie,*Matter* **2020**, *3*, 509–521; b) C. Jia, X. Tan, Y. Zhao, W. Ren, Y. Li, Z. Su, S. C. Smith, C. Zhao, *Angew. Chem. Int. Ed.* **2021**,*60*, 23342–23348.

[25] J. Dong, Y. Liu, J. Pei, H. Li, S. Ji, L. Shi, Y. Zhang, C. Li, C. Tang, J. Liao, S. Xu, H. Zhang, Q. Li, S. Zhao, *Nat. Commun.* **2023**, *14*, 6849.

[26] a) J. Tang, X. Zhao, J. Li, R. Guo, Y. Zhou, J. Liu, *ACS Appl. Mater. Interfaces* **2017**, *9*, 35977–35987; b) G. Kresse, D. Joubert, *Phys. Rev. B* **1999**, *59*, 1758–1775; c) J. P. Perdew, K. Burke, M. Ernzerhof, *Phys. Rev. Lett.* **1996**, *77*, 3865–3868; d) S. Grimme, *J. Comput. Chem.* **2006**, *27*, 1787–1799; e) H. J. Monkhorst, J. D. Pack, *Phys. Rev. B* **1976**, *13*, 5188–5192; f) J. K. Nørskov, J. Rossmeisl, A. Logadottir, L. Lindqvist, J. R. Kitchin, T. Bligaard, H. Jónsson, *J. Phys. Chem. B* **2004**, *108*, 17886–17892; g) J. Rossmeisl, A. Logadottir, J. K. Nørskov, *Chem. Phys.* **2005**, *319*, 178–184.

Manuscript received: November 29, 2023
Accepted manuscript online: December 15, 2023
Version of record online: December 29, 2023